

## Original research articles

## Irregularly sampled seismic data interpolation via wavelet-based convolutional block attention deep learning

Yihuai Lou <sup>a,b</sup>, Lukun Wu <sup>c</sup>, Lin Liu <sup>d</sup>, Kai Yu <sup>e</sup>, Naihao Liu <sup>f,\*</sup>, Zhiguo Wang <sup>g,\*</sup>, Wei Wang <sup>h</sup><sup>a</sup> Center for Hypergravity Experimental and Interdisciplinary Research, Zhejiang University, Hangzhou, Zhejiang 310058, China<sup>b</sup> MOE Key Laboratory of Soft Soils and Geoenvironmental Engineering, College of Civil Engineering and Architecture, Zhejiang University, Hangzhou, Zhejiang 310058, China<sup>c</sup> School of Software Engineering, Xi'an Jiaotong University, Xi'an, Shaanxi 710049, China<sup>d</sup> Petrochina CBM Company Limited, Beijing 100028, China<sup>e</sup> Capitalonline Data Service Co., LTD, Beijing 100012, China<sup>f</sup> School of Information and Communications Engineering, Xi'an Jiaotong University, Xi'an, Shaanxi 710049, China<sup>g</sup> School of Mathematics and Statistics, Xi'an Jiaotong University, Xi'an, Shaanxi 710049, China<sup>h</sup> PowerChina Huadong Engineering Corporation Limited, Hangzhou, Zhejiang 310014, China

## ARTICLE INFO

## Keywords:

Irregularly sampled seismic data reconstruction

Deep learning

U-Net

Discrete wavelet transform

Convolutional block attention module

## ABSTRACT

Seismic data interpolation, especially irregularly sampled data interpolation, is a critical task for seismic processing and subsequent interpretation. Recently, with the development of machine learning and deep learning, convolutional neural networks (CNNs) are applied for interpolating irregularly sampled seismic data. CNN based approaches can address the apparent defects of traditional interpolation methods, such as the low computational efficiency and the difficulty on parameters selection. However, current CNN based methods only consider the temporal and spatial features of irregularly sampled seismic data, which fail to consider the frequency features of seismic data, i.e., the multi-scale features. To overcome these drawbacks, we propose a wavelet-based convolutional block attention deep learning (W-CBADL) network for irregularly sampled seismic data reconstruction. We firstly introduce the discrete wavelet transform (DWT) and the inverse wavelet transform (IWT) to the commonly used U-Net by considering the multi-scale features of irregularly sampled seismic data. Moreover, we propose to adopt the convolutional block attention module (CBAM) to precisely restore sampled seismic traces, which could apply the attention to both channel and spatial dimensions. Finally, we adopt the proposed W-CBADL model to synthetic and pre-stack field data to evaluate its validity and effectiveness. The results demonstrate that the proposed W-CBADL model could reconstruct irregularly sampled seismic data more effectively and more efficiently than the state-of-the-art contrastive CNN based models.

## 1. Introduction

Seismic data reconstruction, which is a tough task, plays an important role in seismic exploration (Chai et al., 2020; Liu et al., 2022b; Bai et al., 2018). Seismic data are often sampled irregularly along the spatial direction due to the constraints on the acquisition condition, the cost limitations, the dead traces, etc (Wang et al., 2020). Irregularly sampled data affects the subsequent seismic processing and interpretation, such as incoherent and coherent noise attenuation (Yuan et al., 2015; Dong et al., 2020; Birnie et al., 2021; Liu et al., 2021c; Yang et al., 2021; Wu et al., 2022c), normal moveout (NMO) correction (Zhang et al., 2013; Biswas et al., 2019; Yuan et al., 2019), seismic inversion (Gao et al., 2016; Wu et al., 2020, 2022b), seismic horizon and

fault interpretation (Wu et al., 2019; Zhou et al., 2020; Wu et al., 2022a), wavefield solution (Alkhalifah et al., 2021; Huang and Alkhalifah, 2022), first arrival picking (Xu et al., 2021; Liu et al., 2021a), etc. It should be noted that incomplete seismic data can be divided into two typical cases, i.e., irregularly sampled seismic data and consecutively sampled seismic data with big gap (Liu et al., 2022b). Moreover, the regularly sampled case is a special case of the irregularly sampled case. Therefore, we only consider the case of irregularly sampled seismic data in this study.

Plenty of methods have been proposed to address seismic data reconstruction, which can be generally divided into traditional approaches and machine learning (ML) based approaches. Traditional

\* Corresponding authors.

E-mail addresses: lou\_yh2021@163.com (Y. Lou), hddsjvae@qq.com (L. Wu), apple1987@petrochina.com.cn (L. Liu), ykkmoon@163.com (K. Yu), naihao\_liu@mail.xjtu.edu.cn (N. Liu), emailwzg@mail.xjtu.edu.cn (Z. Wang), wang\_w20@hdec.com (W. Wang).

reconstruction approaches can be then divided into five categories. The first category is wave equation based approaches, in which seismic interpolation is regarded as an inverse problem (Ronen, 1987; Fomel, 2003). Note that this kind of methods requires the prior knowledge of the velocity model. The second, i.e. prediction error filter (PEF) based approaches (Crawley et al., 1999; Li et al., 2017), utilizes the low-frequency components to predict the linear events at the high-frequency. However, the linearity assumptions of seismic data are not always satisfied, especially for field data. The third one is transform based methods, which transform seismic data to a specific sparse domain and then implement seismic interpolation based on the theory of compressed sensing (Gülinay, 2003; Yu et al., 2007), such as Radon transform (Thorson and Claerbout, 1985; Kabir and Verschuur, 1995), curvelet transform (Herrmann and Hennenfent, 2008; Naghizadeh and Sacchi, 2010), seislet transform (Chen et al., 2014; Gan et al., 2015), dreamlet transform (Wu et al., 2013; Wang et al., 2015), etc. The fourth is based on low-rank assumption of seismic data, in which sampled seismic data can be interpolated by reducing the rank of the analyzed seismic data (Sternfels et al., 2015; Huang and Liu, 2019). However, this kind of methods is difficult to determine the optimal rank, which affects the final interpolation result. The last category is projection-onto-convex-sets (POCS) image reconstruction approaches (Abma and Kabir, 2006; Gao et al., 2013), which are based on the Gerchberg-Saxton iterative algorithm (Trad, 2003), nevertheless, this kind of approaches suffer from the expensive computing cost. Although traditional approaches are proposed to address seismic data reconstruction, they still suffer several apparent limitations. First, these methods often require the prior assumptions, which is difficult to precisely obtain when processing field data. The second limitation is the computational efficiency, especially when facing the massive seismic data. The other one is that users need to manually define plenty of parameters for traditional interpolation methods, and these parameters usually are required to precisely adjust. Certainly, it is a very time-consuming and difficult task to interpolate seismic data at different seismic survey.

Different with theory-driven or model-driven traditional approaches as discussed above, machine learning (ML) based approaches are usually data-driven, which can adaptively build a model for seismic data reconstruction by learning the characteristics of seismic data itself. With the development of ML based models, they are utilized to overcome the limitations of traditional interpolation approaches, such as the pre-assumptions of the linear events, the sparsity, the low rank, etc (Jia and Ma, 2017). In addition, ML based approaches often introduce a trained regression function to guide seismic data interpolation without the manual parameter tuning, which is accurate and computationally efficient. Deep learning (DL), as a branch of ML, has been introduced into seismic exploration, such as seismic fault interpretation (Liu et al., 2020; Li et al., 2022), impedance inversion (Wu et al., 2021; Chen et al., 2021), lithology identification (Lin et al., 2020; Liu et al., 2021b), seismic facies analysis (Zhang et al., 2019; Li et al., 2020), noise attenuation (Dong et al., 2022; Liu et al., 2022a), etc. In recent years, DL based methods have been used for addressing irregularly sampled seismic data reconstruction, the most classic of which is convolutional neural networks (CNNs). For example, Mandelli et al. (2018) used convolutional autoencoders to solve irregularly sampled seismic data reconstruction, first introducing CNNs into deep learning-based seismic interpolation. Park et al. (2019) presented a U-net model trained with common shot gathers for regularly sampled seismic data reconstruction. Wang et al. (2019) designed an eight-layer residual learning network (ResNet) with better deep back-propagation characteristics for interpolating sampled seismic data. Yoon et al. (2020) proposed to reconstruct sampled seismic traces using the recurrent neural network (RNN). Wei et al. (2021) proposed a cGAN model based on the Pix2Pix GAN to interpolate irregularly sampled seismic data.

However, current CNN models only focus on the temporal information of seismic data, failing to consider seismic features in the frequency domain, i.e., the multi-scale features of seismic data. Therefore, the

performance of CNN models could be further improved, especially for reconstructing seismic data with detailed features. The multi-layer wavelet convolutional neural network (MWCNN) has been proposed to address the above issues (Liu et al., 2018). MWCNN adopts discrete wavelet transform (DWT) and inverse discrete wavelet transform (IWT) in U-Net to avoid the information loss caused by the pooling operations. It should be noted that MWCNN uses U-Net as the backbone, which introduces a large number of feature channels in the upsampling part and allows the network to propagate the context information to the high resolution layers (Liu et al., 2022b).

In this study, to effectively utilize the information extracted from seismic data in both time and frequency domains, we propose a wavelet-based convolutional block attention deep learning network (W-CBADL) for irregularly sampled seismic data reconstruction. W-CBADL takes MWCNN as the basic architecture. As pointed previously, compared with U-Net, MWCNN uses DWT to replace the pooling operations in the contracting subnetwork. In CNN-based models, the pooling operation is usually introduced to expand the receptive field, which may destroy the detailed characteristics of seismic reflections, which in turn is not conducive to accurate reconstruction of seismic data (Liu et al., 2022b). By using the downsampling scheme based on the invertibility of DWT when utilizing the multi-scale feature representation, the multi-scale features in both time and frequency domains are extracted, which is conducive to the preservation of detailed features (Liu et al., 2018, 2022b). In the expanding subnetwork, inverse wavelet transform (IWT) is utilized for upsampling the low resolution feature maps to the high resolution ones (Liu et al., 2018). Moreover, the element-wise summation module is adopted to combine the feature maps of the contracting and the expanding subnetworks, which can enrich the multi-scale feature representation and reduce computational burden. Notably, our W-CBADL model introduces a convolutional block attention module (CBAM), which is a state-of-the-art attention mechanism. Traditional attention modules only pay attention to which layers in the channel dimension will have stronger feedback capabilities, but does not reflect the meaning of attention in the spatial dimension. CBAM applies attention to both the channel dimension and the spatial dimension (Woo et al., 2018). On one hand, CBAM facilitates each branch to learn “what” and “where” in the channel and spatial dimensions. On the other hand, the multi-scale features at the time and frequency domains can be precisely represented in the channel and space dimensions. Therefore, CBAM can learn to emphasize or suppress the features at the time and frequency domains obtained by DWT in the channel and spatial dimensions, which is beneficial for obtaining the multi-scale information. Obviously, this is important for reconstructing sampled seismic data. In the following sections, we firstly introduce DWT, IWT, MWCNN, and CBAM in detail. Next, we introduce the detailed architecture of our W-CBADL model. Afterward, we implement the experiments on a synthetic data set and a field data set. Comparing W-CBADL with U-Net and MWCNN in the case of irregularly sampled seismic data, we present their qualitative and quantitative results and the detailed analysis. Finally, we provide the discussions and main conclusions of this study.

## 2. Methodology

### 2.1. Discrete wavelet transform and inverse discrete wavelet transform

Discrete wavelet transform (DWT) is formulated in the late 1980s (Daubechies, 1988). By taking haar wavelet as an example, an image  $x$  can be decomposed into four sub-images using DWT, which are low-pass image  $x_{LL}$  (average) and three high-pass images, including  $x_{HL}$  (horizontal),  $x_{LH}$  (vertical), and  $x_{HH}$  (diagonal). These four decomposed

sub-images are defined as

$$\left\{ \begin{array}{l} \mathbf{x}_{LL}(i, j) = \mathbf{x}(2i - 1, 2j - 1) + \mathbf{x}(2i - 1, 2j) \\ \quad + \mathbf{x}(2i, 2j - 1) + \mathbf{x}(2i, 2j), \\ \mathbf{x}_{LH}(i, j) = -\mathbf{x}(2i - 1, 2j - 1) - \mathbf{x}(2i - 1, 2j) \\ \quad + \mathbf{x}(2i, 2j - 1) + \mathbf{x}(2i, 2j), \\ \mathbf{x}_{HL}(i, j) = -\mathbf{x}(2i - 1, 2j - 1) + \mathbf{x}(2i - 1, 2j) \\ \quad - \mathbf{x}(2i, 2j - 1) + \mathbf{x}(2i, 2j), \\ \mathbf{x}_{HH}(i, j) = \mathbf{x}(2i - 1, 2j - 1) - \mathbf{x}(2i - 1, 2j) \\ \quad - \mathbf{x}(2i, 2j - 1) + \mathbf{x}(2i, 2j), \end{array} \right. \quad (1)$$

where  $\mathbf{x}_{LL}(i, j)$ ,  $\mathbf{x}_{LH}(i, j)$ ,  $\mathbf{x}_{HL}(i, j)$ , and  $\mathbf{x}_{HH}(i, j)$  denote the pixels at the  $j$ th column and the  $i$ th row of  $\mathbf{x}_{LL}$ ,  $\mathbf{x}_{LH}$ ,  $\mathbf{x}_{HL}$ , and  $\mathbf{x}_{HH}$ , respectively.

Obviously, DWT in Eq. (1) can be considered as a convolution operation between  $\mathbf{x}$  and four  $2 \times 2$  filters in strides of 2, described as

$$\left\{ \begin{array}{l} \mathbf{f}_{LL} = \begin{bmatrix} 1 & 1 \\ 1 & 1 \end{bmatrix}, \quad \mathbf{f}_{LH} = \begin{bmatrix} -1 & -1 \\ 1 & 1 \end{bmatrix}, \\ \mathbf{f}_{HL} = \begin{bmatrix} -1 & 1 \\ -1 & 1 \end{bmatrix}, \quad \mathbf{f}_{HH} = \begin{bmatrix} 1 & -1 \\ -1 & 1 \end{bmatrix}. \end{array} \right. \quad (2)$$

Notice that the pixel-size of the four sub-images generated by using DWT is reduced to half of the original image, which can replace the pooling operation (Ronneberger et al., 2015).

Due to the orthogonality of the four filters defined in Eq. (1), we can fully restore the target image by using inverse wavelet transform (IWT). Similarly, IWT can be expressed as an inverse convolution operation, defined as

$$\left\{ \begin{array}{l} \mathbf{x}(2i - 1, 2j - 1) = (\mathbf{x}_{LL}(i, j) - \mathbf{x}_{LH}(i, j) \\ \quad - \mathbf{x}_{HL}(i, j) + \mathbf{x}_{HH}(i, j)) / 4, \\ \mathbf{x}(2i - 1, 2j) = (\mathbf{x}_{LL}(i, j) - \mathbf{x}_{LH}(i, j) \\ \quad + \mathbf{x}_{HL}(i, j) - \mathbf{x}_{HH}(i, j)) / 4, \\ \mathbf{x}(2i - 1, 2j) = (\mathbf{x}_{LL}(i, j) + \mathbf{x}_{LH}(i, j) \\ \quad - \mathbf{x}_{HL}(i, j) - \mathbf{x}_{HH}(i, j)) / 4, \\ \mathbf{x}(2i, 2j) = (\mathbf{x}_{LL}(i, j) + \mathbf{x}_{LH}(i, j) \\ \quad + \mathbf{x}_{HL}(i, j) + \mathbf{x}_{HH}(i, j)) / 4. \end{array} \right. \quad (3)$$

## 2.2. Multi-level wavelet-CNN model

DWT has apparently adaptive spatial frequency resolution, which achieves better spatial resolution at high frequency and better frequency resolution at low frequency (Singh et al., 2011). Moreover, IWT with the orthogonality has been demonstrated to accurately reconstruct the input image. Therefore, we introduce DWT and IWT to preserve the feature maps of the convolutional layers, which can promote the ability and accuracy of seismic data reconstruction.

Liu et al. (2022b) proposed a MWCNN model based on DWT and IWT, which combines wavelet transform and CNNs. As an improved U-Net structure, MWCNN introduces wavelet transform to reduce the size of feature maps in the contracting subnetwork. Furthermore, another convolutional layer is further used to decrease the channels of feature maps, i.e., the expanding subnetwork. Here, IWT is adopted to reconstruct the high resolution feature maps. CNNs typically expand the receptive field at the expense of the computational cost. Although the dilated filtering solves the problem of the high computational cost of CNNs, it suffers from the grid effects and the computed receptive field is only a sparse sampling of the input image with the checkerboard patterns. MWCNN is able to achieve the sizeable receptive fields with the limited computational constraints. Moreover, MWCNN can also be interpreted as a generalization of the dilation filtering and the subsampling, which is beneficial for image restoration tasks.

## 2.3. Convolutional block attention module

Woo et al. (2018) proposed the Convolutional Block Attention Module (CBAM), which is proved to be a simple yet effective attention module for the feed-forward CNNs. CBAM is proposed to improve the 3D feature maps via model training with channel attention and spatial attention (Wang et al., 2021b). CBAM contains two separate sub-modules, which are channel attention module (CAM) and spatial attention module (SAM). Given an intermediate FM  $\mathbf{F} \in \mathbb{R}^{C \times H \times W}$  as the input, CBAM sequentially infers a 1D channel attention map  $\mathbf{M}_c \in \mathbb{R}^{C \times 1 \times 1}$  and a 2D spatial attention map  $\mathbf{M}_s \in \mathbb{R}^{1 \times H \times W}$ , as illustrated in Fig. 1. Thus, the channel-refined FM and the final FM are computed as

$$\left\{ \begin{array}{l} \mathbf{F}' = \mathbf{M}_c(\mathbf{F}) \otimes \mathbf{F}, \\ \mathbf{F}'' = \mathbf{M}_s(\mathbf{F}') \otimes \mathbf{F}', \end{array} \right. \quad (4)$$

where  $\otimes$  denotes the element-wise multiplication.  $\mathbf{F}'$  and  $\mathbf{F}''$  present the channel-refined FM and the final refined FM (Woo et al., 2018). The values are then broadcasted (copied) if the two operands are not with the same dimension, i.e., the spatial attentional values are broadcasted along the channel dimension and the channel attention values are broadcasted along the spatial dimension (Wang et al., 2021a).

### 2.3.1. Channel attention module

To explain CAM, we first apply the average pooling  $f_{ap}$  and the max pooling  $f_{mp}$ . Then, two features  $\mathbf{D}_{ap}$  and  $\mathbf{D}_{mp}$  are computed as

$$\left\{ \begin{array}{l} \mathbf{D}_{ap} = f_{ap}(\mathbf{F}), \\ \mathbf{D}_{mp} = f_{mp}(\mathbf{F}). \end{array} \right. \quad (5)$$

Both  $\mathbf{D}_{ap}$  and  $\mathbf{D}_{mp}$  are sent to a shared multi-layer perceptron (MLP) to produce the output feature maps, which are then merged using the element-wise summation  $\oplus$ . Typically, MLP consists of three layers in Fig. 2(a), including an input layer, a hidden layer, and an output layer. The merged sum is finally sent to the sigmoid function  $\sigma$ , defined as

$$\mathbf{M}_c(\mathbf{F}) = \sigma \{ MLP[\mathbf{D}_{ap}] \oplus MLP[\mathbf{D}_{mp}] \}. \quad (6)$$

To reduce the parameters and simplify the computation, the number of hidden neurons in MLP is set as  $\mathbb{R}^{C/r \times 1 \times 1}$ , where  $r$  is the reduction ratio. Next,  $\mathbf{W}_0 \in \mathbb{R}^{C/r \times C}$  and  $\mathbf{W}_1 \in \mathbb{R}^{C \times C/r}$  are adopted to represent MLP weights. Eq. (6) can be further improved and rewritten as

$$\mathbf{M}_c(\mathbf{F}) = \sigma \{ \mathbf{W}_1 [\mathbf{W}_0(\mathbf{D}_{ap})] \oplus \mathbf{W}_1 [\mathbf{W}_0(\mathbf{D}_{mp})] \}. \quad (7)$$

Note that  $\mathbf{W}_0$  and  $\mathbf{W}_1$  are shared by both  $\mathbf{D}_{ap}$  and  $\mathbf{D}_{mp}$ .

### 2.3.2. Spatial attention module

Fig. 2(b) indicates the simplified architecture of SAM used in this study. Unlike the channel attention, which focuses on “what”, the spatial attention focuses on “where” is the information part, which is complementary to the channel attention (Woo et al., 2018). Here, the average pooling  $f_{ap}$  and the max pooling  $f_{mp}$  are applied to the channel-refined FM  $\mathbf{F}'$ . Next, we have

$$\left\{ \begin{array}{l} \mathbf{E}_{ap} = f_{ap}(\mathbf{F}'), \\ \mathbf{E}_{mp} = f_{mp}(\mathbf{F}'), \end{array} \right. \quad (8)$$

where  $\mathbf{E}_{ap}$  and  $\mathbf{E}_{mp}$  are both two dimensional feature maps and satisfy  $\mathbf{E}_{ap} \in \mathbb{R}^{1 \times H \times W} \wedge \mathbf{E}_{mp} \in \mathbb{R}^{1 \times H \times W}$ .  $\mathbf{E}_{ap}$  and  $\mathbf{E}_{mp}$  are concatenated together along the channel dimension, i.e.,  $\mathbf{E} = concat(\mathbf{E}_{ap}, \mathbf{E}_{mp})$ . Then, the connected activation map is subjected to a standard  $7 \times 7$  convolution operation followed by a sigmoid function  $\sigma$ . Afterward, we obtain

$$\mathbf{M}_s(\mathbf{F}') = \sigma \{ conv[\mathbf{E}] \}. \quad (9)$$

The output  $\mathbf{M}_s(\mathbf{F}')$  is then element-wisely multiplied with  $\mathbf{F}'$ , as defined in Eq. (4).

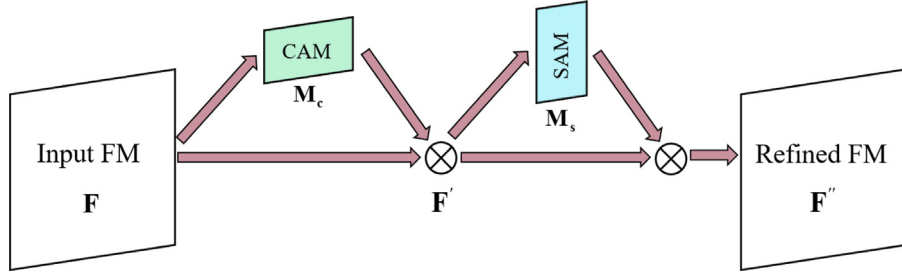


Fig. 1. CBAM and its two sub-modules, i.e., CAM and SAM.

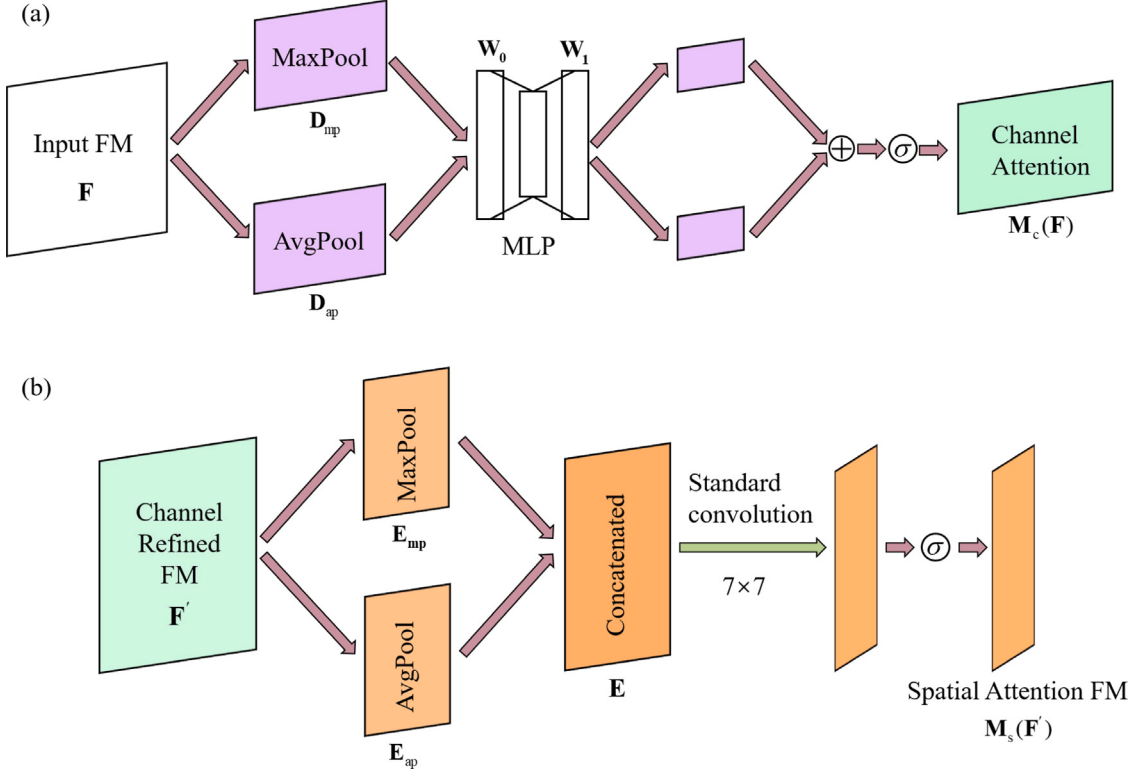


Fig. 2. The simplified architecture of CAM and SAM.

#### 2.4. W-CBADL network

Based on the modules mentioned in the previous sub-sections, we propose a wavelet-based convolutional block attention deep learning (W-CBADL) model for irregularly sampled seismic data reconstruction. Fig. 3 and Table 1 show the simplified architecture and the detailed operations of W-CBADL. The proposed W-CBADL model mainly consists of the encoder, the decoder, and the connection layer (the Add operations in Table 1), which is also a typical U-Net structure. We explain the main parts of the W-CBADL model as follows.

- (1) W-CBADL adopts the DWT and IWT to replace the pooling and general upsampling operations in traditional CNN models. In term of the orthogonality of the wavelet transform, the DWT and IWT can retain more seismic data feature information, which is beneficial for network training and promoting the results of irregularly sampled seismic data reconstruction.
- (2) W-CBADL introduces the convolution block attention module (CBAM). Note that CBAM focuses on distinguishing which layers have stronger feedback capabilities at the channel and spatial

dimensions. CBAM re-calibrates the feature maps by learning a set of weights. The channel attention and spatial attention are also applied to the multi-scale seismic data information obtained by using the DWT and IWT. Thus, the accuracy and effectiveness of irregularly missing seismic data reconstruction can be effectively promoted.

- (3) The W-CBADL model adds the layer information of the corresponding coding layer via the Add operation after each IWT, which can strengthen the feature information. Moreover, its computational cost is lower than the conventional concatenation operation.

#### 3. Synthetic examples

To examine the availability of W-CBADL, we first apply it on synthetic data and implement a case, i.e., irregularly sampled seismic data, which randomly exclude 70% of traces in each patch. Furthermore, we provide qualitative and quantitative comparisons and explanations with state-of-the-art U-Net and MWCNN models.

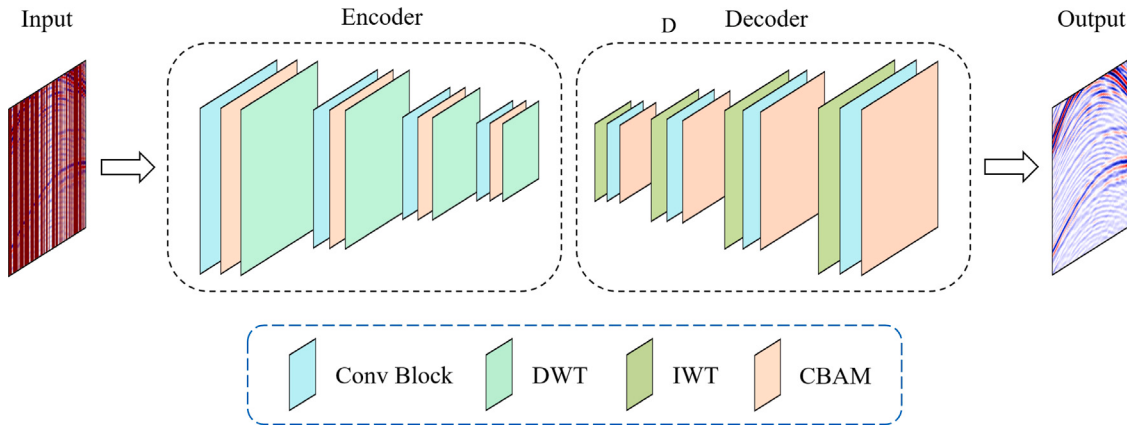


**Fig. 3.** The simplified architecture of the proposed W-CBADL model. The “Conv Block” operation contains two Conv  $3 \times 3$ , Batch Norm, ReLU, refer to the Table 1 for details.

**Table 1**

The detailed operations and hyper-parameters of the proposed W-DBADL model.

Layer name	Operation	Input size	Output size
CB 1	Conv Block	(128, 128, 1)	(128, 128, 32)
CM 1	CBAM	(128, 128, 32)	(128, 128, 32)
DWT 1	DWT	(128, 128, 32)	(64, 64, 128)
CB 2	Conv Block	(64, 64, 128)	(64, 64, 64)
CM 2	CBAM	(64, 64, 64)	(64, 64, 64)
DWT 2	DWT	(64, 64, 64)	(32, 32, 256)
CB 3	Conv Block	(32, 32, 256)	(32, 32, 128)
CM 3	CBAM	(32, 32, 128)	(32, 32, 128)
DWT 3	DWT	(32, 32, 128)	(16, 16, 512)
CB 4	Conv Block	(16, 16, 512)	(16, 16, 256)
CM 4	CBAM	(16, 16, 256)	(16, 16, 256)
DWT 4	DWT	(16, 16, 256)	(8, 8, 1024)
CB 5	Conv Block	(8, 8, 1024)	(8, 8, 512)
CM 5	CBAM	(8, 8, 512)	(8, 8, 512)
CBR 5	Conv $3 \times 3$ , Batch Norm, ReLU	(8, 8, 512)	(8, 8, 1024)
IWT 4	IWT	(8, 8, 1024)	(16, 16, 256)
ADD 4	Add (CM 4, IWT 4)	(16, 16, 256)	(16, 16, 256)
DCB 4	Conv Block	(16, 16, 256)	(16, 16, 256)
DCM 4	CBAM	(16, 16, 256)	(16, 16, 256)
CBR 4	Conv $3 \times 3$ , Batch Norm, ReLU	(16, 16, 256)	(16, 16, 512)
IWT 3	IWT	(16, 16, 512)	(32, 32, 128)
ADD 3	Add (CM 3, IWT 3)	(32, 32, 128)	(32, 32, 128)
DCB 3	Conv Block	(32, 32, 128)	(32, 32, 128)
DCM 3	CBAM	(32, 32, 128)	(32, 32, 128)
CBR 3	Conv $3 \times 3$ , Batch Norm, ReLU	(32, 32, 128)	(32, 32, 256)
IWT 2	IWT	(32, 32, 256)	(64, 64, 64)
ADD 2	Add (CM 2, IWT 2)	(64, 64, 64)	(64, 64, 64)
DCB 2	Conv Block	(64, 64, 64)	(64, 64, 64)
DCM 2	CBAM	(64, 64, 64)	(64, 64, 64)
CBR 2	Conv $3 \times 3$ , Batch Norm, ReLU	(64, 64, 64)	(64, 64, 128)
IWT 1	IWT	(64, 64, 128)	(128, 128, 32)
ADD 1	Add (CM 1, IWT 1)	(128, 128, 32)	(128, 128, 32)
DCB 1	Conv Block	(128, 128, 32)	(128, 128, 32)
DCM 1	CBAM	(128, 128, 32)	(128, 128, 32)
OUT	Conv $1 \times 1$ , Sigmoid	(128, 128, 32)	(128, 128, 1)

### 3.1. Synthetic data set

The synthetic data set used in this study is SEG C3 data set.<sup>1</sup> The time sampling number and interval are 625 and 8 ms, while the spatial interval is 20 m. We randomly select 8000 patches of  $128 \times 128$  from SEG C3 data set and then all extracted patches are normalized as [0,

1] by using the Min–Max normalization, which can be expressed as

$$y = \frac{y_c - \min(y_c)}{\max(y_c) - \min(y_c)}, \quad (10)$$

where  $y_c$  is complete data before normalization, and  $y$  is the normalized data.. Next, we divide these 8000 patches into 50% as training set (4000 patches), 25% as validation set (2000 patches), and remaining 25% as blind test set (2000 patches). Fig. 4 shows several examples of synthetic data.

### 3.2. Model training

DL models are all built with Keras and Tensorflow deep learning library on Python 3.6. Specifically, both Keras and Tensorflow are the version of 2.4.0. All computations are implemented on a graphics processing unit, i.e., NVIDIA GTX 3090 (24 GB GPU memory). These models are all trained with a batch size of 40 and a maximum of 500 epochs to make a trade-off between training efficiency and convergence rate. The commonly used Adam optimizer is selected as optimization algorithm to minimize the loss function. The learning rate is initially set as 0.01. In addition, the activation function and the loss function are set as the Rectified Linear Unit (ReLU) (Nair and Hinton, 2010) and the Mean Square Error (MSE) (Allen, 1971).

After model training, the loss values are presented by the blue, orange, and gray curves in Fig. 5. It should be noted that these loss curves are drawn from the 20-th epoch to facilitate the display of convergence and contrast effects. Obviously, the W-CBAL model and the contrastive DL models both converge. Moreover, in Fig. 5, it can be easily found that W-CBADL converges slowly in the early stage of model training, but accelerates the convergence from the 120-th epoch, and finally converges to a lower value than U-Net and MWCNN. This indicates that, after model training, we obtain a more accurate W-CBADL model than the other two contrastive DL models.

### 3.3. Evaluation matrix

We introduce several evaluation matrices to quantitatively evaluate different DL models, including Peak Signal to Noise Ratio (PSNR) (Huynh-Thu and Ghanbari, 2008), Structure Similarity Index Measure (SSIM) (Wang et al., 2004), Mean Absolute Error (MAE) (Chai and Draxler, 2014), and Mean Absolute Percentage Error (MAPE) (De Myttenaere et al., 2016). Consider that  $x_i$  and  $y_i$  denote the  $i$ th predicted result and corresponding label, while  $n$  represents the number of the samples. These matrices are explained as follows.

*Peak Signal to Noise Ratio (PSNR):*

$$PSNR = 10 \cdot \log_{10} \left( \frac{MAX_I^2}{MSE} \right), \quad (11)$$

<sup>1</sup> [https://wiki.seg.org/wiki/SEG\\_C3\\_NA](https://wiki.seg.org/wiki/SEG_C3_NA)

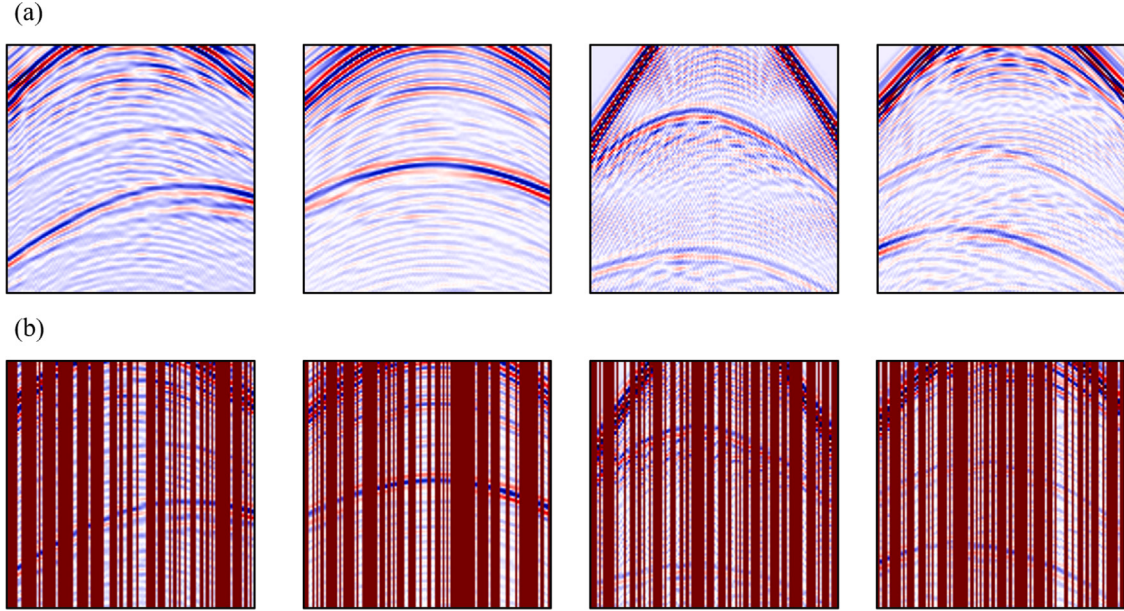


**Fig. 4.** The examples of 70% irregularly sampled synthetic data. (a) The ground truth and (b) the incomplete synthetic data.

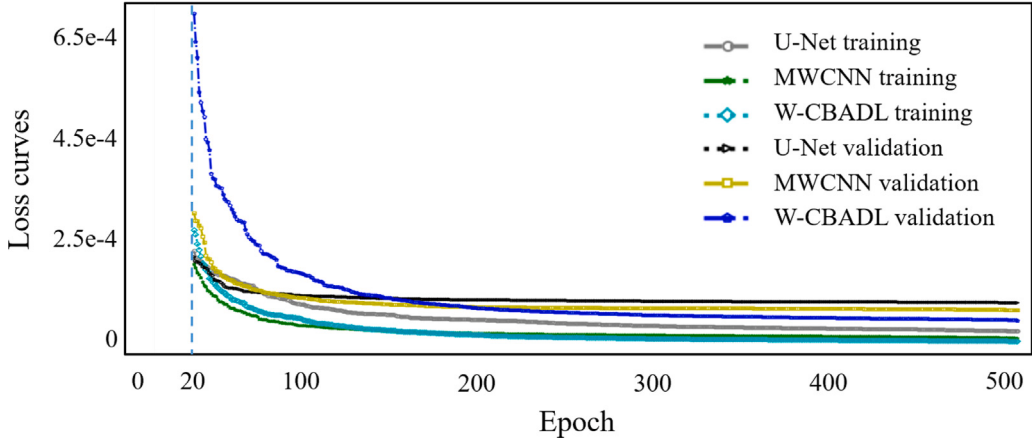


**Fig. 5.** The loss curves for different DL models. The gray circle, green star, and cyan diamond curves denote the training loss of U-Net, MWCNN, and W-CBADL; the black triangle, yellow square, and blue pentagram curves denote the validation loss of U-Net, MWCNN, and W-CBADL.

where  $\text{MAX}_I^2$  denotes the maximum pixel value of the image,  $MSE$  is the mean square error (MSE) between the predicted result and the label. The larger PSNR, the less distortion between the predicted result and the ground truth.

**Structure Similarity Index Measure (SSIM):** SSIM is a measure of similarity between two images (Wang et al., 2004), presented as

$$\text{SSIM}(\mathbf{x}, \mathbf{y}) = \frac{(2\mu_x\mu_y + c_1)(2\sigma_{xy} + c_2)}{(\mu_x^2 + \mu_y^2 + c_1)(\sigma_x^2 + \sigma_y^2 + c_2)}, \quad (12)$$

where  $\mu_x$  and  $\mu_y$  present the averages of  $x$  and  $y$ ,  $\sigma_x^2$  and  $\sigma_y^2$  indicate the variances of  $x$  and  $y$ .  $\sigma_{xy}$  is the covariance of  $x$  and  $y$ .  $c_1 = (k_1 L)^2$  and  $c_2 = (k_2 L)^2$  are the constant values used to maintain the stability, where  $k_1 = 0.01$  and  $k_2 = 0.03$  in this study.  $L$  is the dynamic range of the pixel values. SSIM between two images is between 0 and 1, when SSIM is closer to 1, the reconstructed image has less distortion.

**Mean Absolute Error (MAE):**

$$\text{MAE} = \frac{1}{n} \sum_{i=1}^n |\mathbf{x}_i - \mathbf{y}_i|. \quad (13)$$

When the predicted result is completely consistent with the label, MAE turns to 0, which stands for obtaining a good model. And, the greater the error, the greater the value.

**Mean Absolute Percentage Error (MAPE):**

$$\text{MAPE} = \frac{100\%}{n} \sum_{i=1}^n \left| \frac{\mathbf{x}_i - \mathbf{y}_i}{\mathbf{y}_i} \right|, \quad (14)$$

Note that MAPE is actually a percentage. The smaller MAPE, the better the model effect. It is generally believed that the prediction accuracy is higher when MAPE is less than 10.

### 3.4. Synthetic data results

We apply the fine-tuned models to blind test data set. Fig. 6(a) and 6(b) show ground truth and irregularly sampled synthetic data randomly selected from blind test data set. Fig. 6(f) and 6(g) are their  $f - k$  spectrum. Afterward, Fig. 6(c), 6(d), and 6(e) show the reconstructed results computed using U-Net, MWCNN, and W-CBADL. Meanwhile, the  $f - k$  spectra of U-Net, MWCNN, and W-CBADL are denoted in Fig. 6(h), 6(i), and 6(j). It should be noted that we normalize these  $f - k$  spectra to make the fair contrast. The images

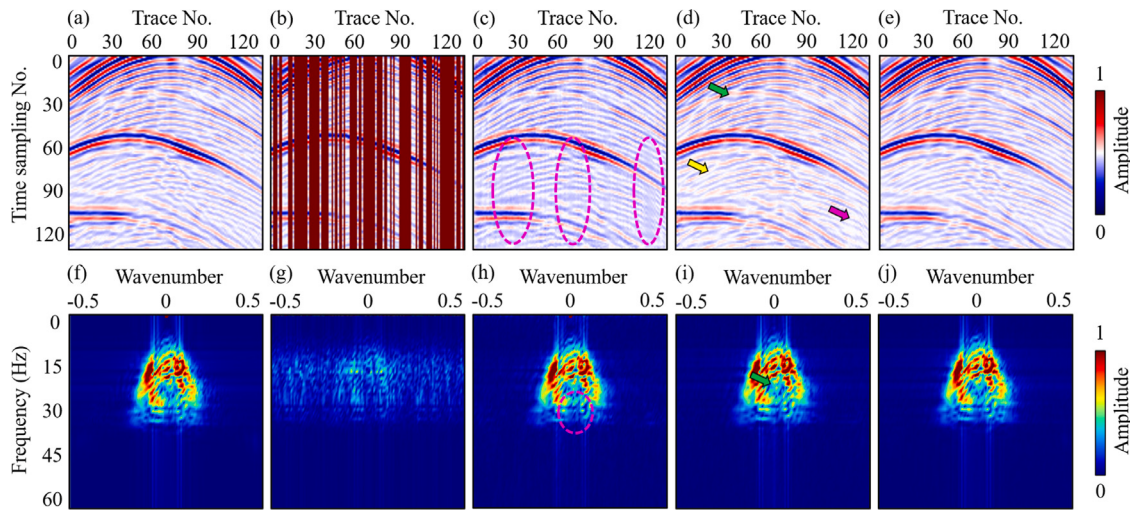


**Fig. 6.** The reconstructed results of irregularly sampled synthetic data based on different DL models. (a) Ground truth, (b) incomplete synthetic data, reconstructed data calculated using (c) U-Net, (d) the MWCNN, (e) W-CBADL, (f)–(j)  $f - k$  spectra, respectively.

reconstructed using different methods in Fig. 6 indicate that there are several limitations existed in current DL models. First, although U-Net can restore seismic valid events, a part of seismic events are still missing. Especially, the pink circles in Fig. 6(c) and 6(h) indicate that it is difficult to restore the irregularly sampled part with big gap. Second, compared with U-Net, MWCNN obtains more complete interpolated results, but a part of seismic valid events are still losing. For example, some weak reflections and sampled traces cannot be precisely reconstructed, highlighted by the yellow and pink cursors in Fig. 6(d). Moreover, the green cursors in Fig. 6(d) and 6(i) denote that there is still an unreasonable relationship between the relative amplitudes of the adjacent traces in the part restored by MWCNN. Finally, W-CBADL achieves the most reasonable results compared to the contrastive DL models, whose interpolated result is the closest to ground truth in Fig. 6(a). Additionally, Fig. 7 show the difference images between the reconstructed results in Fig. 6(c), 6(d), 6(e), 6(h), 6(i), 6(j) and the ground truth in Fig. 6(a), 6(f), respectively. By comparing these images, we have two main observations. First, the difference images of U-Net and MWCNN show apparent visible differences in Fig. 7(a) and 7(b), especially for the irregularly missing area. Obviously, the difference images of their  $f - k$  spectra are larger. This indicates that U-Net and MWCNN fails to accurately reconstruct sampled data. Although the difference image of the proposed model also shows seismic reflection losses in Fig. 7(c) and 7(f), these losses are visibly less than those of U-Net and MWCNN, benefiting from the time and spatial perception property of CBAM. Second, the difference images of U-Net and MWCNN show different mean value shifts, while the former larger than 0 and the later smaller than 0. This means that these two models cannot maintain seismic valid reflections when interpolating the missing reflections. Nevertheless, note that there is not mean value shift in Fig. 7(c) and 7(f), demonstrating the availability of W-CBADL for reconstructing the sampled data and preserving the original seismic reflections.

To further verify the interpolation performance of W-CBADL, we show 1D seismic examples of irregularly sampled synthetic data, which are extracted from the first row in Fig. 6(a) and the trace number is 102. In Fig. 8(b), we zoom in the presented traces by the red rectangle in Fig. 8(a). It can be clearly observed that the restored trace of W-CBADL, denoted by the blue diamond curve, is the closest to ground truth presented by the red curve, which is superior to the other two restored traces calculated by using the contrastive DL models. Next, the aforementioned evaluation matrices are calculated by using different DL models, shown in Table 2. It should be noted that the higher SSIM and PSNR correspond to more suitable DL model, while the lower MAE and MAPE are related with more accurate DL model.

**Table 2**

Comparisons of different models on irregularly sampled synthetic data.

Model	MAE	SSIM	PSNR	MAPE
U-Net	1.1735e-02	0.9519	37.4345	2.2772
MWCNN	6.1965e-03	0.9711	40.7333	1.2464
W-CBADL	4.1270e-03	0.9778	43.0520	0.8337

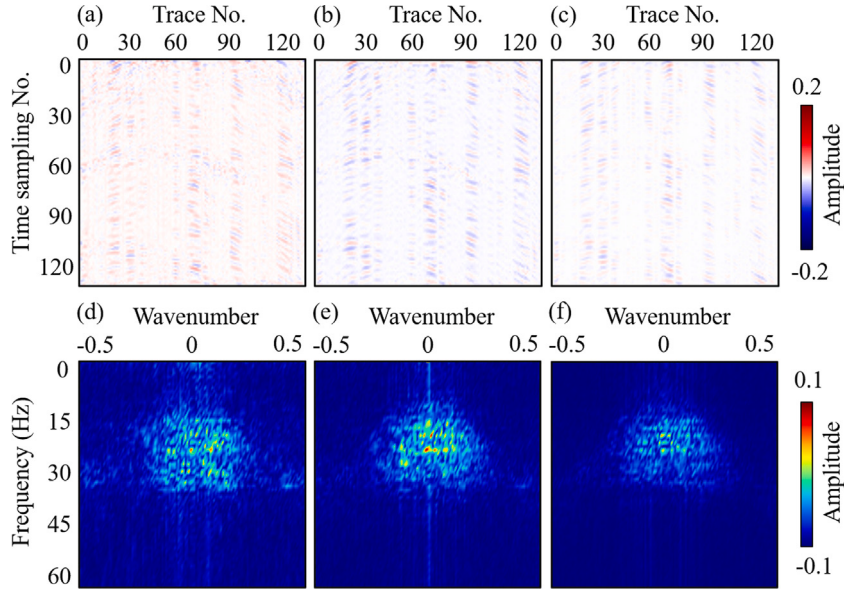
The comparing result of the evaluation matrices in Table 2 indicates that the proposed W-CBADL model achieves the best performance on all evaluation matrices, which further verifies its effectiveness. After the above analysis, we can conclude that W-CBADL is significantly better than the comparative DL models in qualitative and quantitative evaluations, which proves its superiority and availability for seismic data reconstruction.

#### 4. Field applications

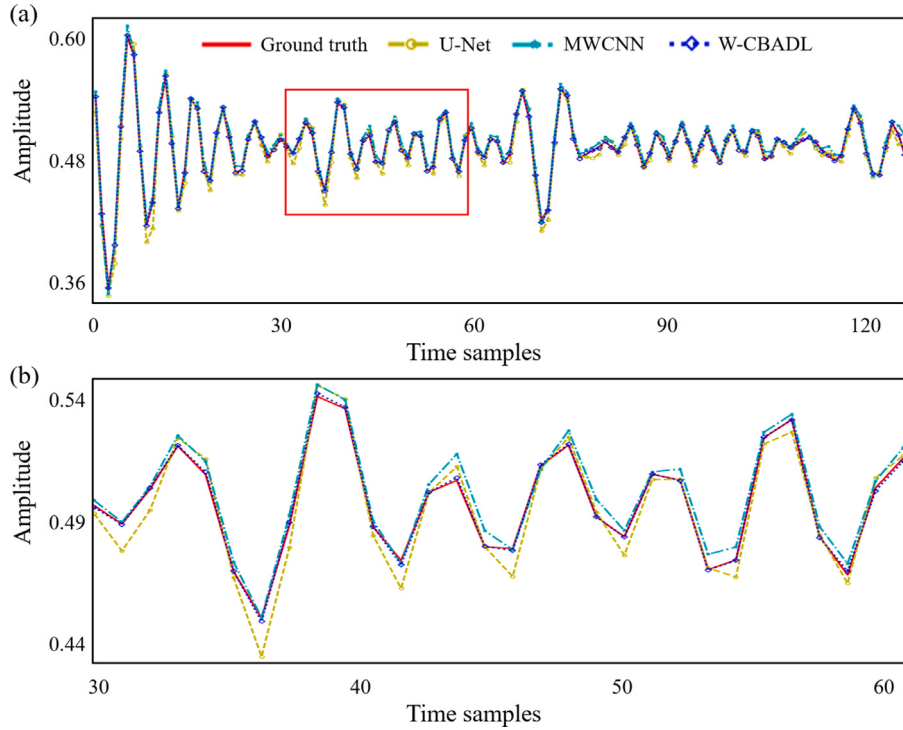
We further adopt field data set to verify the effectiveness of the proposed model and make detailed comparisons with state-of-the-art DL models. For field data set, we randomly select 4000 patches from the Mobil Avo Viking Graben Line 12 field data set,<sup>2</sup> each of which has a size of  $512 \times 112$ , which are different with synthetic data set. Note that the spatial sampling interval and the time sampling interval are 25 m and 4 ms. Next, we divide the selected 4000 patches into 2000, 1000, and 1000, i.e., 50% as training set, 25% as validation set, and 25% as blind test set. The images in Fig. 9 indicate several 70% irregularly sampled field data examples, which is randomly selected from training data set. Afterward, we aim to adopt different DL models to reconstruct these incomplete field data.

Fig. 10 and Table 3 denote the results acquired by applying different DL models on irregularly sampled field data for qualitative and quantitative comparisons. The reconstruction results shown in Fig. 10 indicate that there are several limitations existed in current DL models, and the reconstruction performance of our proposed W-CBADL model is superior than U-Net and MWCNN. First, the red cursor and the circle in Fig. 10(c) highlight that U-Net has difficulty on preserving seismic valid events at the bottom and produces the significant distortion in the missing part. Moreover, the pink cursor in Fig. 10(c) presents that the restored part still has a significant amplitude loss. Second, compared with U-Net, MWCNN can retain more seismic valid events,

<sup>2</sup> [https://wiki.seg.org/wiki/Mobil\\_AVO\\_viking\\_graben\\_line\\_12](https://wiki.seg.org/wiki/Mobil_AVO_viking_graben_line_12)



**Fig. 7.** The difference images between the reconstructed results in Fig. 6(c), 6(d), 6(e), 6(h), 6(i), 6(j) and the ground truth in Fig. 6(a), 6(f), respectively.



**Fig. 8.** (a) The synthetic traces extracted from Fig. 6 with the trace number of 102 and (b) the enlarged part highlighted by the red rectangle in (a). The red solid, yellow circle, cyan star, and blue diamond curves denote ground truth and restored traces computed using U-Net, MWCNN, and W-CBADL, respectively.

whereas there is still a significant gap with ground truth in Fig. 10(a). It should be noted that the image in Fig. 10(d) also has the incomplete restoration of seismic valid events, indicated by the pink cursor and the circles. Third, seismic valid events restored by W-CBADL are more continuous, more complete, and more reasonable than those restored by U-Net and MWCNN. Furthermore, the  $f-k$  spectra in Fig. 10 lead to the similar conclusion. Apparently, the  $f-k$  spectra of the reconstructed results computed using the U-Net and MWCNN models show significant amplitude errors, as represented by the pink circle in Fig. 10(h) and 10(i). Whereas, W-CBADL has the smallest error compared with the ground truth  $f-k$  spectrum, i.e., Fig. 10(j) is almost identical to Fig. 10(f). Furthermore, Fig. 11 denote the difference images between

the reconstructed results in Fig. 10(h), 10(i), 10(j) and the ground truth in Fig. 10(f). The difference results of the proposed W-CBADL model are obviously with less error than the difference results of the compared DL model. In addition, compared with U-Net and MWCNN, W-CBADL achieves higher SSIM and PSNR and lower MAE and MAPE, which can be easily found in Table 3. Therefore, W-CBADL performs best on all quantitative matrices, which proves its superiority. The above descriptions show that W-CBADL is an effective model for restoring the irregularly sampled seismic data.

Furthermore, We further zoom in the corresponding part denoted by the blue rectangle in Fig. 10(b) and show the cropped image in Fig. 12. The comparisons in Fig. 12 also indicate that the reconstruction

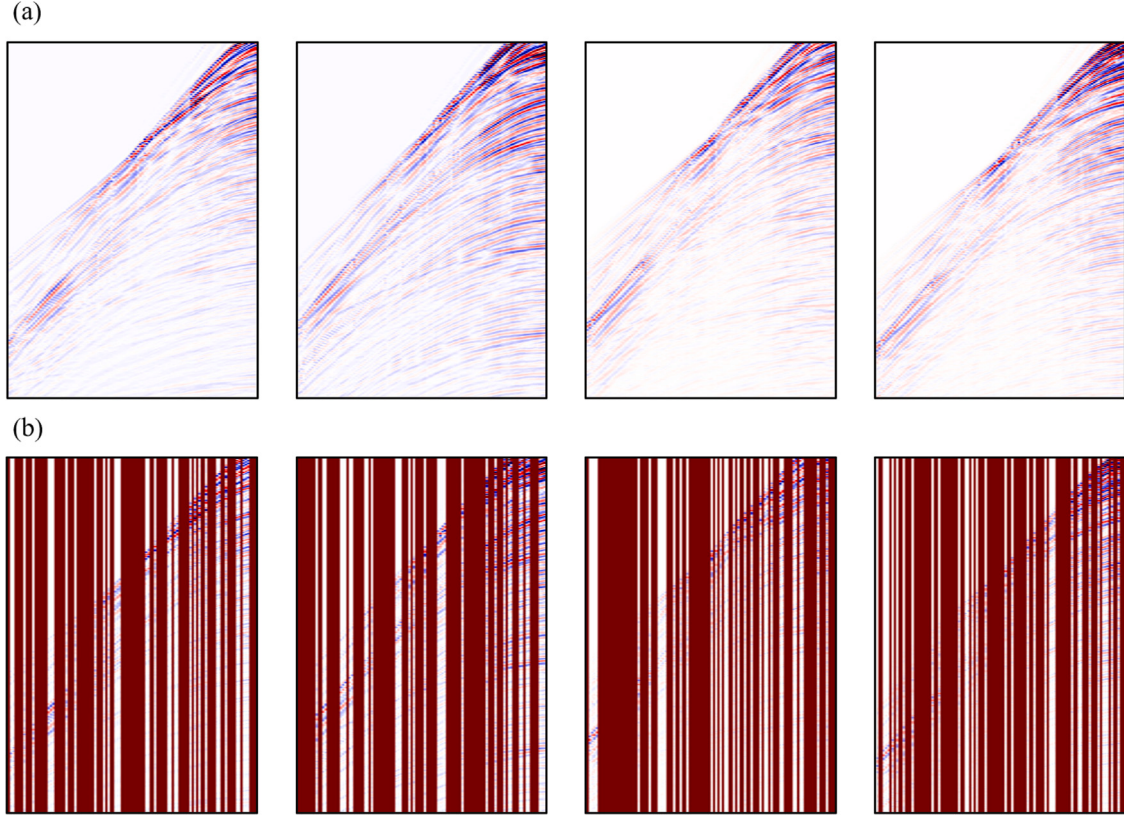


**Fig. 9.** The examples of 70% irregularly sampled field data. (a) Ground truth and (b) incomplete field data.

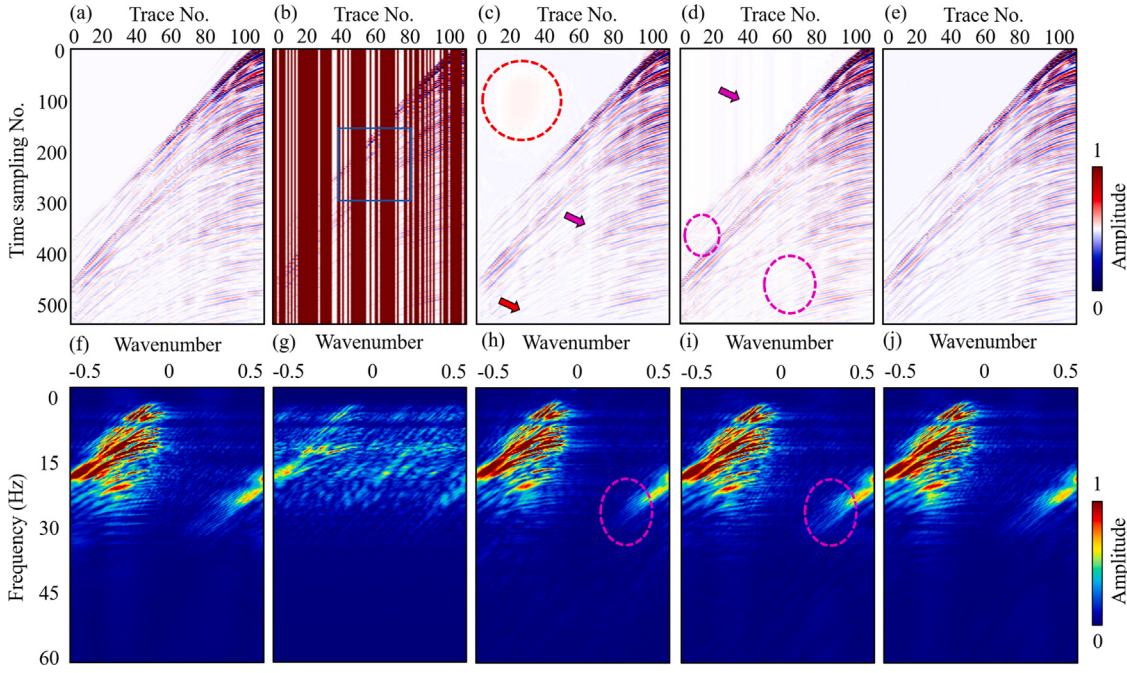


**Fig. 10.** The reconstruction results of different DL models on the irregularly sampled field data. (a) Ground truth, (b) irregularly sampled field data, reconstructed data computed using (c) U-Net, (d) MWCNN, (e) W-CBADL; (f)–(j) the corresponding  $f-k$  spectra.

performance of our proposed W-CBADL is superior than U-Net and MWCNN. First, the pink cursor and the circle in Fig. 12(c) represent that, although U-Net can preserve seismic valid events, the preserved traces are discontinuous and unreasonable. Second, the pink circle and

the yellow cursor in Fig. 12(d) denote that MWCNN restores more seismic valid events than U-Net, but still has significant amplitude losses and some weak reflection losses. Finally, seismic valid events restored by W-CBADL are the closest to ground truth in Fig. 12(a) and

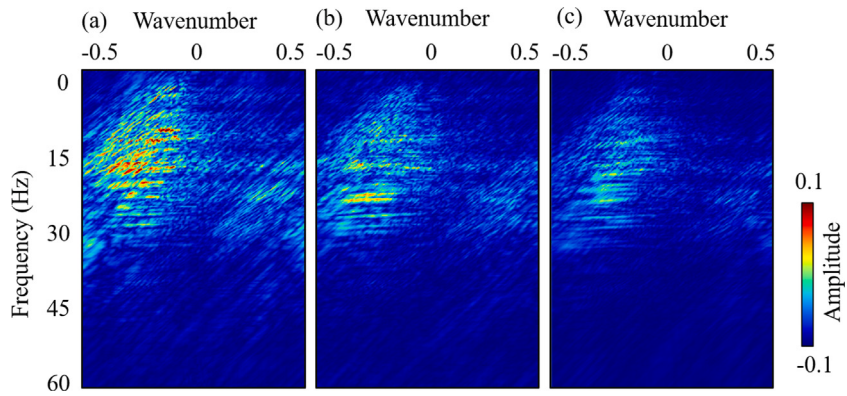


**Fig. 11.** The difference images between the reconstructed results in Fig. 10(h), 10(i), 10(j) and the ground truth in Fig. 10(f).

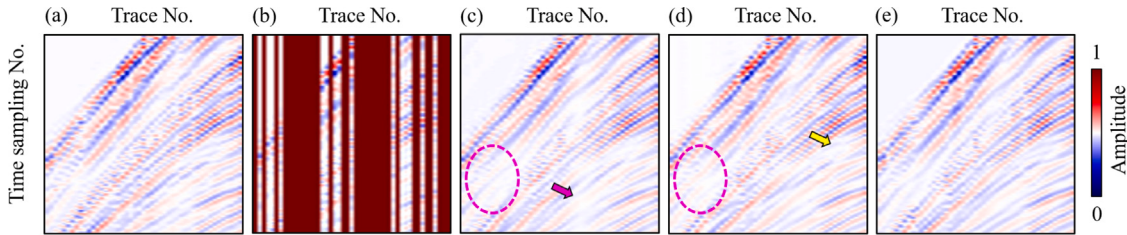


**Fig. 12.** The zoomed reconstruction results denoted by the blue rectangle in Fig. 10(b). (a) Ground truth, (b) irregularly sampled field data, reconstructed data predicted using (c) U-Net, (d) MWCNN, and (e) W-CBADL, respectively.

**Table 3**

Comparisons of different models on irregularly sampled field data.

Model	MAE	SSIM	PSNR	MAPE
U-Net	3.3364e-03	0.9734	43.3247	0.7060
MWCNN	3.0002e-03	0.9832	44.9421	0.6076
W-CBADL	2.2755e-03	<b>0.9899</b>	<b>45.7441</b>	<b>0.4620</b>

achieves the most reasonable result in Fig. 12(e). All of the above compared results fully illustrate the versatility, superiority, and reliability of W-CBADL on irregularly sampled seismic data reconstruction.

## 5. Conclusion

We propose and train a wavelet-based convolutional block attention deep learning network (W-CBADL) to interpolate irregularly sampled seismic data. First, W-CBADL combines the wavelet transform with traditional CNNs. On one hand, the multi-scale characteristic of DWT and IWT boosts the accuracy of W-CBADL for seismic data reconstruction. On the other hand, W-CBADL can restore the target image nondestructively by utilizing the orthogonality of wavelet transform. Next, W-CBADL further introduces a convolutional block attention module (CBAM). We utilize the CBAM to distinguish which feature maps have stronger feedback capabilities in both channel and spatial dimensions. Then, we prepare training data sets which are consisted of synthetic and field seismic data. Finally, the comparison results demonstrate that W-CBADL outperforms U-Net and MWCNN both quantitatively and qualitatively. Moreover, we verify the feasibility, effectiveness, and superiority of the proposed W-CBADL on irregularly sampled seismic data reconstruction, especially for irregularly sampled parts with big gaps and weak reflections.

## Declaration of competing interest

The authors declare that they have no known competing financial interests or personal relationships that could have appeared to influence the work reported in this paper.

## Acknowledgments

This research was supported by the National Natural Science Foundation of China under Grant 42274144 and under Grant 41974137. The authors express their gratitude to the Sandia National Laboratory and Mobil Oil Company for the open data. The authors deeply appreciate the valuable comments from Associate Editor and another three anonymous reviewers.

## References

- Abma, R., Kabir, N., 2006. 3D interpolation of irregular data with a POCS algorithm. *Geophysics* 71 (6), E91–E97.
- Alkhalifah, T., Song, C., bin Waheed, U., Hao, Q., 2021. Wavefield solutions from machine learned functions constrained by the Helmholtz equation. *Artif. Intell. Geosci.* 2, 11–19.
- Allen, D.M., 1971. Mean square error of prediction as a criterion for selecting variables. *Technometrics* 13 (3), 469–475.
- Bai, X., Chen, J., Yuan, S., Wei, S., Wang, X., Wang, J., 2018. Study on seismic data acquisition and processing technology of shale gas of complex mountainous in South China —Taking the analysis of Gui-Guang's 2D seismic exploration as an example. *Unconventional Oil Gas* 5 (02), 1–8.
- Birnie, C., Ravasi, M., Liu, S., Alkhalifah, T., 2021. The potential of self-supervised networks for random noise suppression in seismic data. *Artif. Intell. Geosci.* 2, 47–59.
- Biswas, R., Vassiliou, A., Stromberg, R., Sen, M.K., 2019. Estimating normal moveout velocity using the recurrent neural network. *Interpretation* 7 (4), T819–T827.
- Chai, T., Draxler, R.R., 2014. Root mean square error (RMSE) or mean absolute error (MAE)—Arguments against avoiding RMSE in the literature. *Geosci. Model Dev.* 7 (3), 1247–1250.
- Chai, X., Tang, G., Wang, S., Lin, K., Peng, R., 2020. Deep learning for irregularly and regularly missing 3-D data reconstruction. *IEEE Trans. Geosci. Remote Sens.* 59 (7), 6244–6265.
- Chen, Y., Chen, K., Shi, P., Wang, Y., 2014. Irregular seismic data reconstruction using a percentile-half-thresholding algorithm. *J. Geophys. Eng.* 11 (6), 065001.
- Chen, H., Gao, J., Zhang, W., Yang, P., 2021. Seismic acoustic impedance inversion via optimization-inspired semisupervised deep learning. *IEEE Trans. Geosci. Remote Sens.* 60, 1–11.
- Crawley, S., Clapp, R., Claerbout, J., 1999. Interpolation with smoothly nonstationary prediction-error filters. In: SEG Technical Program Expanded Abstracts 1999. Society of Exploration Geophysicists, pp. 1154–1157.
- Daubechies, I., 1988. Orthonormal bases of compactly supported wavelets. *Comm. Pure Appl. Math.* 41 (7), 909–996.

- De Myttenaere, A., Golden, B., Le Grand, B., Rossi, F., 2016. Mean absolute percentage error for regression models. *Neurocomputing* 192, 38–48.
- Dong, X., Lin, J., Lu, S., Huang, X., Wang, H., Li, Y., 2022. Seismic shot gather denoising by using a supervised-deep-learning method with weak dependence on real noise data: A solution to the lack of real noise data. *Surv. Geophys.* 1–32.
- Dong, X., Zhong, T., Li, Y., 2020. New suppression technology for low-frequency noise in desert region: The improved robust principal component analysis based on prediction of neural network. *IEEE Trans. Geosci. Remote Sens.* 58 (7), 4680–4690.
- Fomel, S., 2003. Seismic reflection data interpolation with differential offset and shot continuation. *Geophysics* 68 (2), 733–744.
- Gan, S., Wang, S., Chen, Y., Zhang, Y., Jin, Z., 2015. Dealiasing seismic data interpolation using seislet transform with low-frequency constraint. *IEEE Geosci. Remote Sens. Lett.* 12 (10), 2150–2154.
- Gao, Z., Pan, Z., Gao, J., 2016. Multimutation differential evolution algorithm and its application to seismic inversion. *IEEE Trans. Geosci. Remote Sens.* 54 (6), 3626–3636.
- Gao, J., Stanton, A., Naghizadeh, M., Sacchi, M.D., Chen, X., 2013. Convergence improvement and noise attenuation considerations for beyond alias projection onto convex sets reconstruction. *Geophys. Prospect.* 61, 138–151.
- Gülnay, N., 2003. Seismic trace interpolation in the Fourier transform domain. *Geophysics* 68 (1), 355–369.
- Herrmann, F.J., Hennenfent, G., 2008. Non-parametric seismic data recovery with curvelet frames. *Geophys. J. Int.* 173 (1), 233–248.
- Huang, X., Alkhalifah, T., 2022. PINNup: Robust neural network wavefield solutions using frequency upscaling and neuron splitting. *J. Geophys. Res.: Solid Earth* 127 (6), e2021JB023703.
- Huang, W., Liu, J., 2019. Robust seismic image interpolation with mathematical morphological constraint. *IEEE Trans. Image Process.* 29, 819–829.
- Huynh-Thu, Q., Ghanbari, M., 2008. Scope of validity of PSNR in image/video quality assessment. *Electron. Lett.* 44 (13), 800–801.
- Jia, Y., Ma, J., 2017. What can machine learning do for seismic data processing? An interpolation application. *Geophysics* 82 (3), V163–V177.
- Kabir, M.N., Verschuur, D., 1995. Restoration of missing offsets by parabolic radon transform 1. *Geophys. Prospect.* 43 (3), 347–368.
- Li, C., Liu, G., Hao, Z., Zu, S., Mi, F., Chen, X., 2017. Multidimensional seismic data reconstruction using frequency-domain adaptive prediction-error filter. *IEEE Trans. Geosci. Remote Sens.* 56 (4), 2328–2336.
- Li, S., Liu, N., Li, F., Gao, J., Ding, J., 2022. Automatic fault delineation in 3-D seismic images with deep learning: Data augmentation or ensemble learning? *IEEE Trans. Geosci. Remote Sens.* 60, 1–14.
- Li, F., Zhou, H., Wang, Z., Wu, X., 2020. ADDCNN: An attention-based deep dilated convolutional neural network for seismic facies analysis with interpretable spatial-spectral maps. *IEEE Trans. Geosci. Remote Sens.* 59 (2), 1733–1744.
- Liu, J., Li, H., Liu, N., Gao, J., Li, Z., 2020. Automatic lithology identification by applying LSTM to logging data: A case study in X tight rock reservoirs. *IEEE Geosci. Remote Sens. Lett.* 18 (8), 1361–1365.
- Liu, N., Chen, J., Wu, H., Li, F., Gao, J., 2021a. Microseismic first-arrival picking using fine-tuning feature pyramid networks. *IEEE Geosci. Remote Sens. Lett.* 19, 1–5.
- Liu, N., He, T., Tian, Y., Wu, B., Gao, J., Xu, Z., 2020. Common-azimuth seismic data fault analysis using residual UNet. *Interpretation* 8 (3), SM25–SM37.
- Liu, N., Huang, T., Gao, J., Xu, Z., Wang, D., Li, F., 2021b. Quantum-enhanced deep learning-based lithology interpretation from well logs. *IEEE Trans. Geosci. Remote Sens.* 60, 1–13.
- Liu, N., Li, F., Wang, D., Gao, J., Xu, Z., 2021c. Ground-roll separation and attenuation using curvelet-based multichannel variational mode decomposition. *IEEE Trans. Geosci. Remote Sens.* 60, 1–14.
- Liu, N., Wang, J., Gao, J., Chang, S., Lou, Y., 2022a. Similarity-informed self-learning and its application on seismic image denoising. *IEEE Trans. Geosci. Remote Sens.* 60, 1–13.
- Liu, N., Wu, L., Wang, J., Wu, H., Gao, J., Wang, D., 2022b. Seismic data reconstruction via wavelet-based residual deep learning. *IEEE Trans. Geosci. Remote Sens.* 60, 1–13.
- Liu, P., Zhang, H., Zhang, K., Lin, L., Zuo, W., 2018. Multi-level wavelet-CNN for image restoration. In: Proceedings of the IEEE Conference on Computer Vision and Pattern Recognition Workshops. pp. 773–782.
- Mandelli, S., Borra, F., Lipari, V., Bestagini, P., Sarti, A., Tubaro, S., 2018. Seismic data interpolation through convolutional autoencoder. In: SEG Technical Program Expanded Abstracts 2018. Society of Exploration Geophysicists, pp. 4101–4105.
- Naghizadeh, M., Sacchi, M.D., 2010. Beyond alias hierarchical scale curvelet interpolation of regularly and irregularly sampled seismic data. *Geophysics* 75 (6), WB189–WB202.
- Nair, V., Hinton, G.E., 2010. Rectified linear units improve restricted boltzmann machines. In: Icm.
- Park, J., Yoon, D., Seol, S.J., Byun, J., 2019. Reconstruction of seismic field data with convolutional U-Net considering the optimal training input data. In: SEG Technical Program Expanded Abstracts 2019. Society of Exploration Geophysicists, pp. 4650–4654.
- Ronen, J., 1987. Wave-equation trace interpolation. *Geophysics* 52 (7), 973–984.
- Ronneberger, O., Fischer, P., Brox, T., 2015. U-Net: Convolutional networks for biomedical image segmentation. In: International Conference on Medical Image Computing and Computer-Assisted Intervention. Springer, pp. 234–241.
- Singh, P., Singh, P., Sharma, R.K., 2011. JPEG image compression based on biorthogonal, coiflets and daubechies wavelet families. *Int. J. Comput. Appl.* 13 (1), 1–7.
- Sternfels, R., Viguerie, G., Gondoin, R., Le Meur, D., 2015. Multidimensional simultaneous random plus erratic noise attenuation and interpolation for seismic data by joint low-rank and sparse inversion. *Geophysics* 80 (6), WD129–WD141.
- Thorson, J., Claerbout, J., 1985. Velocity stack and slant stochastic inversion: Geophysics. Soc. Expl. Geophys. 50, 2727–2741.
- Trad, D., 2003. Interpolation and multiple attenuation with migration operators. *Geophysics* 68 (6), 2043–2054.
- Wang, Z., Bovik, A.C., Sheikh, H.R., Simoncelli, E.P., 2004. Image quality assessment: From error visibility to structural similarity. *IEEE Trans. Image Process.* 13 (4), 600–612.
- Wang, S.-H., Fernandes, S.L., Zhu, Z., Zhang, Y.-D., 2021a. AVNC: Attention-based VGG-style network for COVID-19 diagnosis by CBAM. *IEEE Sens. J.* 22 (18), 17431–17438.
- Wang, Y., Wang, B., Tu, N., Geng, J., 2020. Seismic trace interpolation for irregularly spatial sampled data using convolutional autoencoder. *Geophysics* 85 (2), V119–V130.
- Wang, B., Wu, R.-S., Chen, X., Li, J., 2015. Simultaneous seismic data interpolation and denoising with a new adaptive method based on dreamlet transform. *Geophys. J. Int.* 201 (2), 1182–1194.
- Wang, B., Zhang, N., Lu, W., Wang, J., 2019. Deep-learning-based seismic data interpolation: A preliminary result. *Geophysics* 84 (1), V11–V20.
- Wang, S.-H., Zhou, Q., Yang, M., Zhang, Y.-D., 2021b. ADVIAN: Alzheimer's disease VGG-inspired attention network based on convolutional block attention module and multiple way data augmentation. *Front. Aging Neurosci.* 13, 313.
- Wei, Q., Li, X., Song, M., 2021. Reconstruction of irregular missing seismic data using conditional generative adversarial networks. *Geophysics* 86 (6), V471–V488.
- Woo, S., Park, J., Lee, J.-Y., Kweon, I.S., 2018. Cbam: Convolutional block attention module. In: Proceedings of the European Conference on Computer Vision. ECCV, pp. 3–19.
- Wu, R.-S., Geng, Y., Ye, L., 2013. Preliminary study on Dreamlet based compressive sensing data recovery. In: SEG Technical Program Expanded Abstracts 2013. Society of Exploration Geophysicists, pp. 3585–3590.
- Wu, H., Li, Z., Liu, N., 2022a. Variable seismic waveforms representation: Weak-supervised learning based seismic horizon picking. *J. Pet. Sci. Eng.* 110412.
- Wu, B., Meng, D., Wang, L., Liu, N., Wang, Y., 2020. Seismic impedance inversion using fully convolutional residual network and transfer learning. *IEEE Geosci. Remote Sens. Lett.* 17 (12), 2140–2144.
- Wu, X., Shi, Y., Fomel, S., Liang, L., Zhang, Q., Yusifov, A.Z., 2019. FaultNet3D: Predicting fault probabilities, strikes, and dips with a single convolutional neural network. *IEEE Trans. Geosci. Remote Sens.* 57 (11), 9138–9155.
- Wu, B., Xie, Q., Wu, B., 2022b. Seismic impedance inversion based on residual attention network. *IEEE Trans. Geosci. Remote Sens.* 60, 1–17.
- Wu, X., Yan, S., Bi, Z., Zhang, S., Si, H., 2021. Deep learning for multidimensional seismic impedance inversion. *Geophysics* 86 (5), R735–R745.
- Wu, H., Zhang, B., Liu, N., 2022c. Self-adaptive denoising net: Self-supervised learning for seismic migration artifacts and random noise attenuation. *J. Pet. Sci. Eng.* 110431.
- Xu, k., Lv, J., Pei, G., Li, P., Zhong, H., Liu, Y., 2021. Study on the application of seismic first arrival pickup method in complex piedmont. *Unconv. Oil Gas* 8 (04), 1–10.
- Yang, Y., Wang, Z., Gao, J., Liu, N., Li, Z., 2021. Sparse inversion-based seismic random noise attenuation via self-paced learning. *Artif. Intell. Geosci.* 2, 223–233.
- Yoon, D., Yeeh, Z., Byun, J., 2020. Seismic data reconstruction using deep bidirectional long short-term memory with skip connections. *IEEE Geosci. Remote Sens. Lett.* 18 (7), 1298–1302.
- Yu, Z., Ferguson, J., McMechan, G., Anno, P., 2007. Wavelet-Radon domain dealiasing and interpolation of seismic data. *Geophysics* 72 (2), V41–V49.
- Yuan, E., Chen, F., Qi, Z., Long, J., 2015. Research and application of SVD in separation of special interference wave. *Unconv. Oil Gas* 2 (05), 20–25.
- Yuan, S., Wei, W., Wang, D., Shi, P., Wang, S., 2019. Goal-Oriented Inversion-Based NMO Correction Using a Convex  $l_{2,1}$ -Norm. *IEEE Geosci. Remote Sens. Lett.* 17 (1), 162–166.
- Zhang, Y., Liu, Y., Zhang, H., Xue, H., 2019. Seismic facies analysis based on deep learning. *IEEE Geosci. Remote Sens. Lett.* 17 (7), 1119–1123.
- Zhang, B., Zhang, K., Guo, S., Marfurt, K.J., 2013. Nonstretching NMO correction of prestack time-migrated gathers using a matching-pursuit algorithm. *Geophysics* 78 (1), U9–U18.
- Zhou, R., Cai, Y., Zong, J., Yao, X., Yu, F., Hu, G., 2020. Automatic fault instance segmentation based on mask propagation neural network. *Artif. Intell. Geosci.* 1, 31–35.